minerals

MDPI

Article

Revisiting Glauconite Geochronology: Lessons Learned from In Situ Radiometric Dating of a Glauconite-Rich Cretaceous Shelfal Sequence

Esther Scheiblhofer [1,†], Ulrike Moser [1,*,†], Stefan Löhr [2,3], Markus Wilmsen [4], Juraj Farkaš [3], Daniela Gallhofer [5], Alice Matsdotter Bäckström [6], Thomas Zack [3,6] and Andre Baldermann [1]

[1] Institute of Applied Geosciences, NAWI Graz Geocenter, Graz University of Technology, Rechbauerstraße 12, 8010 Graz, Austria; esther.scheiblhofer@student.tugraz.at (E.S.); baldermann@tugraz.at (A.B.)
[2] Department of Earth Sciences, Macquarie University, North Ryde, Sydney, NSW 2109, Australia; stefan.loehr@mq.edu.au
[3] Metal Isotope Group (MIG), Department of Earth Sciences, University of Adelaide, North Terrace, Adelaide, SA 5005, Australia; juraj.farkas@adelaide.edu.au (J.F.); thomas.zack@gu.se (T.Z.)
[4] Senckenberg Naturhistorische Sammlungen Dresden, Museum für Mineralogie und Geologie, Königsbrücker Landstr. 159, 01109 Dresden, Germany; markus.wilmsen@senckenberg.de
[5] Institute of Geosciences, University of Graz, NAWI Graz Geocenter, Universitätsplatz 3, 8010 Graz, Austria; daniela.gallhofer@uni-graz.at
[6] Department of Earth Sciences, University of Gothenburg, Guldhedsgatan 5a, 41320 Gothenburg, Sweden; gusalicba@student.gu.se
* Correspondence: ulrike.moser@unileoben.ac.at; Tel.: +43-3842-402-1206
† These authors contributed equally to this work.

Abstract: The scarcity of well-preserved and directly dateable sedimentary sequences is a major impediment to inferring the Earth's paleo-environmental evolution. The authigenic mineral glauconite can potentially provide absolute stratigraphic ages for sedimentary sequences and constraints on paleo-depositional conditions. This requires improved approaches for measuring and interpreting glauconite formation ages. Here, glauconite from a Cretaceous shelfal sequence (Langenstein, northern Germany) was characterized using petrographical, geochemical (EMP), andmineralogical (XRD) screening methods before in situ Rb-Sr dating via LA-ICP-MS/MS. The obtained glauconite ages (~101 to 97 Ma) partly overlap with the depositional age of the Langenstein sequence (±3 Ma), but without the expected stratigraphic age progression, which we attribute to detrital and diagenetic illitic phase impurities inside the glauconites. Using a novel age deconvolution approach, which combines the new Rb-Sr dataset with published K-Ar ages, we recalculate the glauconite bulk ages to obtain stratigraphically significant 'pure' glauconite ages (~100 to 96 Ma). Thus, our results show that pristine ages can be preserved in mineralogically complex glauconite grains even under burial diagenetic conditions (T < 65 °C; <1500 m depth), confirming that glauconite could be a suitable archive for paleo-environmental reconstructions and direct sediment dating.

Keywords: glauconite; radiometric dating; in situ Rb-Sr geochronology; diagenesis; illitization; LA-ICP-MS/MS

Citation: Scheiblhofer, E.; Moser, U.; Löhr, S.; Wilmsen, M.; Farkaš, J.; Gallhofer, D.; Bäckström, A.M.; Zack, T.; Baldermann, A. Revisiting Glauconite Geochronology: Lessons Learned from In Situ Radiometric Dating of a Glauconite-Rich Cretaceous Shelfal Sequence. *Minerals* **2022**, *12*, 818. https://doi.org/10.3390/min12070818

Academic Editor: Pierre Giresse

Received: 25 May 2022
Accepted: 23 June 2022
Published: 27 June 2022

1. Introduction

The physical, mineralogical, and chemical/isotopic characteristics of sedimentary sequences document the co-evolution of life and the earth system through time and space, but the precise dating and correlation of geographically distant localities are often challenging, which limits the applicability of most sedimentary archives for paleo-environmental reconstructions [1,2]. Indeed, the scarcity of precisely datable volcanic ash deposits [3] and organic-rich black shales [4] in the geological record as well as their close

association with specific tectonic and environmental settings, such as active continental margins or anoxic deep-marine basins [5,6], currently limit the accurate dating of marine sediments and the establishment of high-resolution element/isotope records [7,8]. A directly dateable, widespread, and robust mineral archive, which forms at or immediately after the time of sediment deposition, is needed to resolve details on proxy signal evolution (e.g., magnesium, calcium, silicon, sulfur, or oxygen isotopes) in marine sediments throughout the rock record. However, most authigenic minerals (e.g., carbonates and phosphates, both biotic and inorganic), which grow at the water–sediment interface or during early diagenesis are relatively soluble and highly reactive and thus prone to post-depositional alteration via, e.g., erosion and mechanical reworking, microbiological activity, chemical dissolution, re-crystallization, and/or formation of mineral (over)growths [9,10]. These processes often lead to the resetting of the primary or pristine marine signatures linked to sediment/mineral formation, thus limiting their value in paleo-environmental reconstructions, even if these materials are sufficiently well-preserved to be accurately dated [11,12].

The authigenic clay mineral glauconite, in contrast, potentially represents a more robust and directly dateable archive of seawater composition, provided that glauconite formation ages can be accurately measured and interpreted. Glauconite is a dioctahedral 2:1 ferruginous green clay mineral, which is thought to form through the Fe^{3+}-smectite to glauconite reaction (henceforth called glauconitization) during early marine diagenesis [13–18]. Its genesis near the water–sediment interface is controlled mainly by the composition of the sediment substrate, such as fecal pellets, foraminifera chambers, and biogenic/detrital debris, which provide semi-confined micro-environments suitable for glauconitization in calcareous and siliciclastic sequences [19,20]. Moreover, if the rate-limiting chemical elements for glauconite formation, such as $Fe^{2+/3+}$ and K^+ ions, are readily supplied from seawater or porewater, glauconite minerals mature from the nascent (<4 wt.% K_2O), through slightly evolved (4–6 wt.% K_2O), and evolved (6–8 wt.% K_2O) to the highly evolved (>8 wt.% K_2O) stage [13,21].

While the physical and chemical controls linked to the formation of glauconite minerals in marine sediments have been resolved in sufficient detail, the specific timing of glauconitization remains currently disputed. To illustrate, according to Odin and Matter [13], evolved glauconite requires ~10^5 to 10^6 years to form in permeable shelfal sediments, whereas Meunier and El Albani [22] argue that glauconite formation proceeds more slowly in less permeable or deep-marine lithologies, requiring a maturation lasting a few million years (~5 Ma). Recent work on glauconite authigenesis in shallow-water [23] vs. deep-marine [17] settings basically support both interpretations, with slower formation rates potentially problematic for glauconite-based geochronology and a precise dating of marine sediments or sedimentary rocks.

In this contribution, we consider the following two scenarios for the interpretation of glauconite ages (Figure 1). Scenario 1 involves fast (<1 Ma) and complete glauconitization taking place at the seawater–sediment interface, ref. [13] to produce glauconite grains with a homogenous composition and a small age variation, thus fairly well recording the time of sedimentation (Figure 1, left panel). Scenario 2 (Figure 1, right panel) considers slow (>5 Ma) and incomplete glauconitization [22] to generate glauconite grains with a heterogenous composition and a variable age distribution due to their discontinuous growth and maturation at the sediment–seawater interface, leading to the presence of residual substrate components and only partial equilibration with seawater [24]. The presence of such inherited, detrital minerals (e.g., muscovite and K-feldspar) and/or the post-depositional and burial diagenetic growth of illitic clay minerals (e.g., illite and illite-smectite) inside the glauconite grains can potentially modify the bulk glauconite formation ages, shifting them towards younger or older ages, respectively. For example, while some glauconites may yield absolute formation ages close to the expected bio-stratigraphic age of the host sediment (within assigned analytical uncertainties), many glauconite samples are

too young, which has resulted in a general withdrawal of glauconite geochronology [25–27].

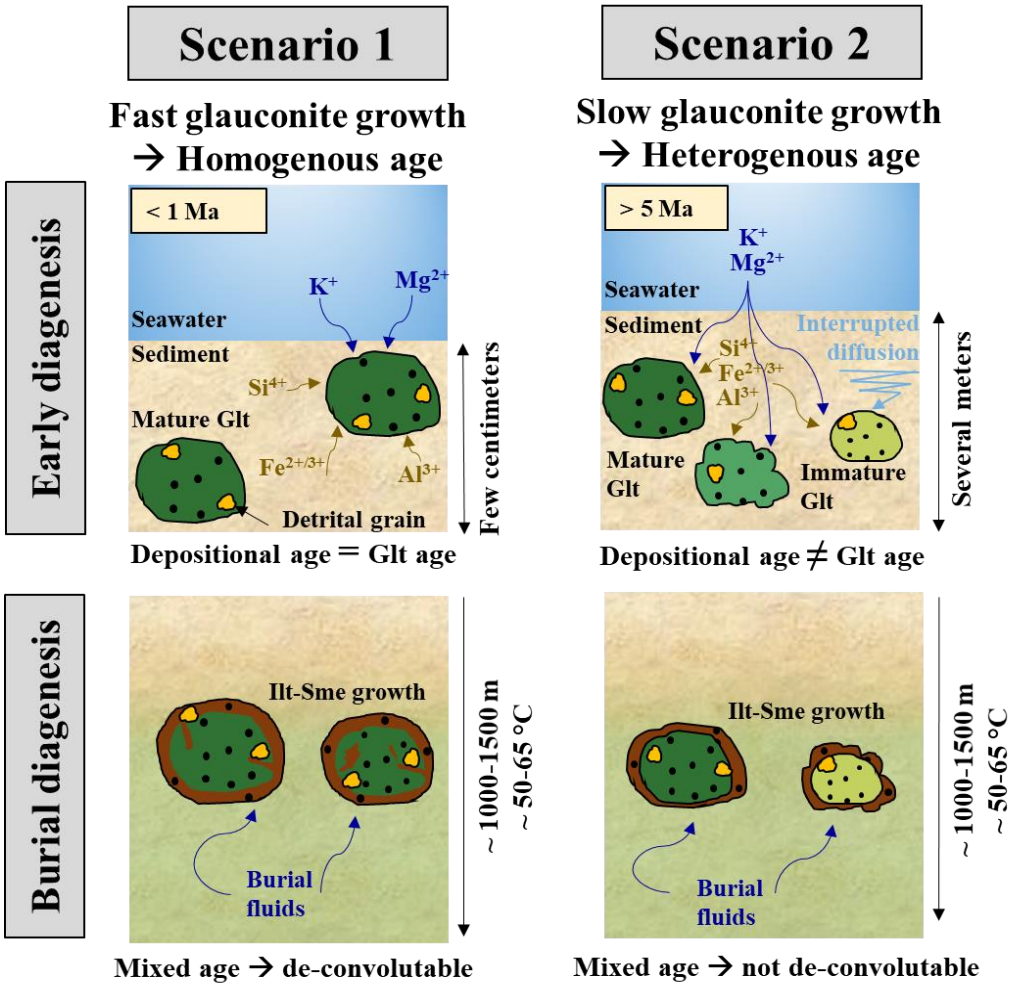

Figure 1. Schematic illustration of rapidly vs. slowly progressing glauconite (Glt) formation in shallow-marine sediments with corresponding effects on glauconite formation ages: Scenario 1 (**left panel**) assumes that the glauconite formation age is coeval or about equal to the sediment depositional age due to fast glauconitization at the sediment–seawater interface [13]. Scenario 2 (**right panel**) anticipates that the glauconite formation age is different compared to the sediment depositional age, reflecting the complexity of seawater/porewater evolution and local glauconite/sediment substrate interactions during slow glauconitization within the sedimentary column [22]. In both cases, the diagenetic intergrowth of illitic phases and the presence of inherited detrital grains can further affect the glauconite bulk ages.

However, depending on the specific conditions prevailing during glauconite formation and potential post-depositional alteration, it may be possible to correct these bulk glauconite ages.

Specifically, if (i) burial diagenesis does not alter the pristine composition and isotopic ratios of the glauconite grains, i.e., in a closed system where Rb and Sr are not mobilized or reset; and (ii) the formation of the glauconite and diagenetic illite proceeds fast (i.e., scenario 1); and (iii) both phases, as well as any other detrital components, can be physically separated, quantified, and radiometrically dated (e.g., via Rb-Sr, K-Ca, K-Ar, or ^{40}Ar-^{39}Ar dating), one could obtain meaningful ages for all mineral components, including authigenic as well as diagenetic and detrital phases. In contrast, if one or more generations of the diagenetic minerals form slowly over a long period of time (i.e., a few Ma) or progressively replace the detrital phases (scenario 2), then the resultant 'mixed' ages

cannot be easily deconvoluted and are barely meaningful for the reconstruction of depositional ages and/or basin history and evolution.

Here, we use authigenic glauconite from the bio-stratigraphically well-constrained Langenstein profile (Subhercynian Cretaceous Basin on the Northern German shelf) of early Late Cretaceous (Cenomanian) age to test the above hypotheses by combining petrographic and mineralogical characterization of the glauconite-rich strata with novel in-situ Rb-Sr dating and chemical analysis of glauconite separated by laser ablation collision cell inductively coupled plasma mass spectrometry analyses (LA-ICP-MS/MS).

2. Materials and Methods

2.1. Material

Glauconite-rich marine sedimentary rocks from the Langenstein profile (Figure 2a), located in the Subhercynian Cretaceous Basin north of the Harz Mountains in northern Germany, were collected during two field campaigns in October 2020 and July 2021. The samples were taken from the entire glauconite-bearing interval, which covers large parts of the Mantelliceras dixoni Zone (Figure 2b), henceforth called M. dixoni Zone (M. dixoni is the index ammonite for the late Early Cenomanian), and the lowermost part of the lower Middle Cenomanian (A. rhotomagense Zone; see Wright and Kennedy [28] for Cenomanian ammonite biozonation). Unconformably overlying lowermost Cretaceous sandstones, the Langenstein section starts with a ferruginous basal transgression conglomerate free of glauconite, which grades into an inner shelf sandstone rich in glauconite (up to 70 wt.%), which is overlain by glauconite-bearing, marls, and marly limestones of the M. dixoni Zone, which accumulated in a mid-shelf setting ([29,30]. These so-called Glauconitic Pläner Limestones contain ~25 to 30 wt.% glauconite in the bottom part and ~1 to 5 wt.% glauconite up-section in the profile. The strongly glauconitic lower part of the section has been previously assigned to the M. dixoni Zone by several authors ([29,31], even if index fossils are absent in this part. Facies change to scarcely glauconitic Pläner Limestones occurs ca. 3.5–4 m above the transgression conglomerate, accompanied by the occurrence of the lower Middle Cenomanian index ammonite of the A. rhotomagense Zone shortly above [29,31]. Up-section, almost glauconite-free pelagic limestones of the late Middle Cenomanian age occur, characterizing the Cenomanian outer shelf facies ([30]. Interventionary studies involving animals or humans, and other studies that require ethical approval, must list the authority that provided approval and the corresponding ethical approval code.

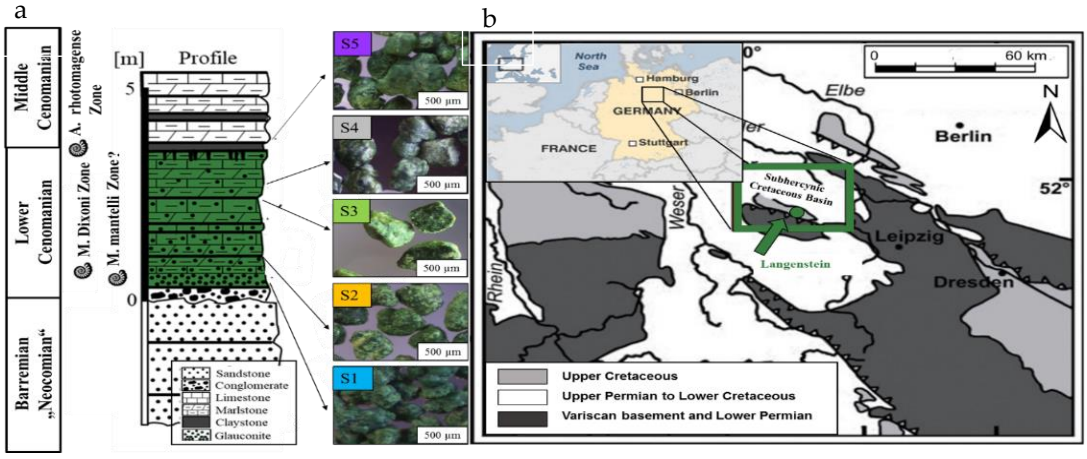

Figure 2. The lithostratigraphic log (**a**) (modified after Baldermann et al. [16]) includes the glauconite-bearing section marked in green color, which probably started in the M. mantelli Zone (S1), passing into the well-defined M. dixoni Zone (S2–S4) and reaching the basal A. rhotomagense Zone, from which theuppermost sample (S5) was collected. Geological overview (**b**) of the studied Langenstein profile, located within the Subhercynian Cretaceous Basin north of the Harz Mountains in Germany (map modified after Voigt et al. ([32,33]).

Two distinct procedures were used for the glauconite extraction and separation: (i) In the case of the glauconite-bearing sandstone (S1 in Figure 2b), a hand-sized specimen was disintegrated by pressing the weakly consolidated or even loose material against a glass plate. (ii) In the case of the glauconite-bearing limestones (S2–S5 in Figure 2b), the carbonate matrix was dissolved using 10% HCl, followed by washing of the acid-insoluble residue with ultrapure water. The loose materials were wet-sieved using standard sieves with different mesh sizes to collect the size fractions larger than 750 μm, 400 μm, 100 μm, and 63 μm and smaller than 63 μm, respectively. Based on an initial mineralogical analysis and an optical microscopic inspection of the collected grain size sub-fractions, it turned out that the glauconite grains from the fraction below 100 μm show evidence of oxidative alteration, i.e., Fe-(hydr)oxides were identified on the exterior and inside cracks within the glauconite grains. Thus, only glauconite grains larger than 100 μm in size without visible signs of alteration were separated using a neodymium magnet and prepared on standard mounts with a tweezer under an optical microscope. Subsequently, the mounts were embedded in epoxy resin (EpoFix resin and EpoFix hardener) and polished using a Pelcon polishing machine (Pelcon Materials & Testing Aps, Ballerup, Denmark) and Struers DP-suspension (Struers GmbH, Willich, Germany) with varying particle size diameter down to 1 μm in preparation for radiometric dating and chemical analysis via LA-ICP-MS/MS (Agilent, Santa Clara, CA, United States).

2.2. Analytical Methods

X-ray diffraction (XRD) patterns were obtained on powdered bulk rock samples using a PANalytical X'Pert PRO diffractometer outfitted with a high-speed Scientific X'Celerator detector (40 kV, 40 mA; Co-Kα radiation source) (Malvern Panalytical Ltd., Malvern, United Kingdom). The top-loading technique was used for sample preparation. The samples were analyzed in the 4 to 85° 2θ range with a step size of 0.008° 2θ and a scan speed of 40 s. Mineral identification was made by Rietveld analysis of the XRD patterns using the PANalytical X'Pert HighScore Plus (version 3.0d (3.0.4)) Software and the ICSD database [34]. For the further identification of mineral impurities present within the glauconites, such as detrital muscovite and diagenetic illite-smectite, the glauconite grains from samples S1–S4 (S5 barely contained glauconite and was therefore not analyzed) were prepared as randomly oriented powder mounts and X-rayed at ambient temperature. Afterward, the preparations were placed in a storage compartment within a desiccator that contained ethylene glycol to induce swelling of the smectitic impurities and reanalyzed followed by Rietveld refinement of the XRD patterns for mineral phase quantification.

The petrography of selected glauconite grains (samples S1–S4) was analyzed on polished thick sections obtained from bulk rock samples by electron microprobe (EMP) analyses using a JEOL JXA8530F Plus Hyper Probe (Jeol Ltd., Tokyo, Japan) at the University of Graz. Mineral impurities present within the glauconite grains were screened and visualized by means of backscatter electron (BSE) images obtained from polished mounts. Chemical data were acquired from individual zones and areas within the impure glauconite grains for mineral identification (see Supplementary Figure S1).

In situ Rb-Sr dating and chemical composition analysis of polished glauconite grain mounts were realized by LA-ICP MS/MS at the Earth Science Center, University of Gothenburg. The isobaric overlap of ^{87}Rb on ^{87}Sr was resolved by applying a reaction cell technology (online separation of ^{87}Sr from ^{87}Rb using a gas) via the recommended reaction gas N_2O to produce SrO^+ along with unreacted Rb^+ ions in the LA system for subsequent dating by ICP-MS/MS at masses 103 and 87 (monitored as 85), respectively [34–37]. To ensure sufficient data reproducibility, only visually homogenous glauconite grains devoid of obvious alteration minerals or mineral inclusions were considered and pre-selected for Rb-Sr age dating, which was carried out on an Agilent 8800QQQ ICP-MS/MS connected to a 213NWR LA system [38]. However, we note that the presence of sub-surface inclusions in glauconite, as well as detrital and diagenetic mineral intergrowths at the sub-micron scale, cannot be excluded, which could affect the bulk glauconite age.

Instrumental configurations are as follows: 50 μm laser spot size, 10 Hz pulse repetition rate, 5.7 J/cm² fluence, and a dwell time of 40 s total or 0.01 s for each mass. The flow rates of the reaction and carrier gases were set to 4 mL N_2/min (22% N_2O), 0.06 mL H_2/min, and 750 mL He/min. Further analytical conditions and instrumental parameters are provided by Hogmalm et al. [37]. For the calibration of the mass response and the calculation of the glauconite ages as well as glauconite compositions the following primary reference materials and external standards were analyzed after each ~10 LA spots on glauconite grains: NIST SRM 610, BCR-2G, Mica-Mg, GA-1150, La Posta, Högsbo-ms, MDC, and Mica-Fe [36,38–46]. They were always reproduced within the 2σ-uncertainty of the recommended values provided by Zack and Hogmalm [39].

The sample and standard average count rates (CPS) of all elements and relevant isotopes were processed with Iolite—Igor Pro© ([47] to determine all important isotopic and element ratios and to enhance the accuracy of the results by adjusting peaks for each measured sample in terms of the program-calculated ratios. A data reduction scheme (DRS) was applied to all ratios, such as Rb^{87}/Sr^{86} and Sr^{87}/Sr^{86} ratios, which considers 2 sigma errors as well as an $^{87}Sr/^{86}Sr$ initial of 0.7074 (i.e., Cenomanian seawater $^{87}Sr/^{86}Sr$ composition [48]) and the primary reference material BCR-2G as well as the secondary standard NIST SRM 610 [39,49]. The DRS and all calculations therein are reported in Rösel and Zack [49]. Sample and standard ages, internal uncertainties (2 sigma errors) and mean square of the weighted deviates (MSWD) were calculated from isochrons produced via the online version of IsoplotR [50–52] and using the updated Rb decay constant of 1.3975 ± 0.0045 (10–11 y^{-1}) reported by Villa et al. [53]. A compilation of relevant datasets obtained from the above standards, reference materials, and glauconites is provided in Supplementary Table S1.

Major element abundances (wt.%) were calculated via an in-house spreadsheet, based on Excel©, using the standardized Longerich equation [54], where the measured Si content was used for normalization. These chemical data were compared with published glauconite compositions based on EMP measurements [55]. However, we note that a direct comparison between the two datasets is challenging, because (i) the chemical data were obtained from different areas within the glauconite grains (thin section vs. glauconite separates), (ii) spot diameters are different (~1.5 vs. 50 μm), and (iii) data processing algorithms and standardization differ among the two methods.

3. Results and Discussion

3.1. Petrography and Geochemistry of Glauconites from Langenstein

Glauconite grains occur in two distinct lithologies at Langenstein, including (i) a ~40 cm thin glauconitic sandstone bed at the base and (ii) glauconite-bearing marly limestones of ~2.5 m vertical thickness in the middle part of the profile (see Figure 2), which document the onset and the progression of the Cenomanian transgression in the Northern German Basin [29]. The glauconite content decreases from ~70 wt.% at the base and ~25 to 10 wt.% in the middle part to <5 wt.% at the top of the profile.

The vast majority of the glauconites appear as dark to medium green-colored, rounded to oval-shaped, and partially cracked grains (~85 wt.% of the total glauconite fraction), ~63 to 500 μm in size (average size: ~200 μm), which are interpreted as glauconitized fecal pellets. Light green-colored fecal pellets (~10 wt.%) as well as greenish foraminifera infills (~5 wt.%) occur in minor proportions. The majority of the green grains are well-sorted and show expansion cracks at the exterior of the glauconites, which is typical for authigenic, highly evolved glauconite [13,15,18,56–58]. Most of the glauconite grains contain detrital quartz, K-feldspar, and illite/muscovite particles as well as hydroxyl-apatite and calcite inclusions; some are filled with secondary minerals, such as Fe-(hydr)oxides, and plenty of grains are intergrown with fine illite-smectite, especially along the surface (micro) cracks (Figure 3a,b). The latter phases likely formed syn- or post-depositional and during burial diagenesis, respectively [16,18,59–61].

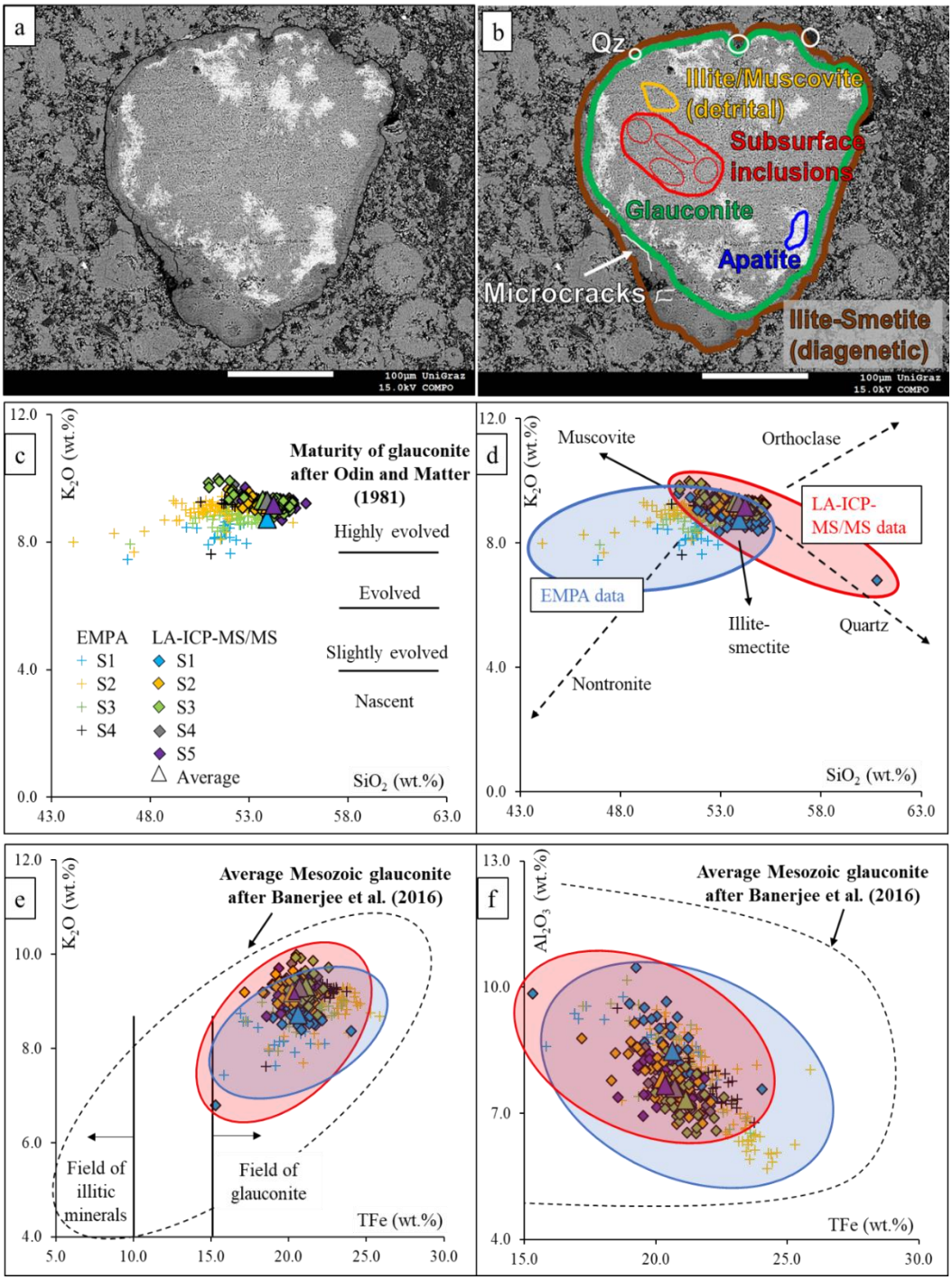

Figure 3. (**a**,**b**) BSE image showing a glauconitized (highly evolved) fecal pellet with abundant apatite (Ap), quartz (Qz), and sub-surface mineral inclusions as well as diagenetic illite-smectite (Ilt-Sme) growing in cracked and fractured areas at the glauconite exterior (rimmed corrosion layer). (**c**–**f**) Cross-plots of major elements in glauconite measured by EMP (blue field/ellipse) and LA-ICP-MS/MS (red field/ellipse). Note that the Langenstein glauconites are evolved to be highly evolved, Fe-rich, and plot well in the range of documented glauconite compositions of the Mesozoic age [13,15]. A strong co-variation in the chemical data is seen, as indicated by an 80% data overlap (2 SD). However, some of the LA-ICP-MS/MS data show evidence of the presence of mineral impurities (see distinct chemical trends highlighted in (**d**)).

Chemically, glauconitization is often described as a transformation reaction of K-poor, Fe(III)-smectite precursors to K- and Fe(III)-rich glauconite via the formation of glauconite-smectite intermediates [19]. Accordingly, published EMP results obtained

from the Langenstein glauconites (samples S1–S4) reveal that these can be characterized as evolved to highly evolved and Fe-rich, judging from the range of measured K_2O and total Fe (TFe: Fe_2O_3 + FeO) contents, with the averages often exceeding approximately 8–9 wt.% and 20–25 wt.%, respectively (Figure 3c,e; [55]. The SiO_2, Al_2O_3, MgO, Na_2O, and CaO contents are inconspicuous and generally plot well within the documented range of Mesozoic glauconites (Figure 3e,f; [15]), as shown by a compositional variability from $(K_{0.75–0.82}Na_{0–0.01}Ca_{0.01–0.04})(Fe^{3+}{}_{1.06–1.20}Fe^{2+}{}_{0.11–0.12}Al_{0.29–0.42}Mg_{0.40–0.46})[Al_{0.27–0.36}Si_{3.65–3.73}O_{10}](OH)_2$ [55].

The chemical compositions of the glauconite grains (S1–S5) measured by LA-ICP-MS/MS analysis (see Supplementary Table S2) range from 50.9 to 60.8 wt.% SiO_2, 6.5 to 10.5 wt.% Al_2O_3, 15.3 to 24.0 wt.% TFe, 3.0 to 4.9 wt.% MgO, and 6.8 to 10.0 wt.% K_2O among all samples studied. Minor amounts belong to Na_2O (0.02–0.05 wt.%) and CaO (0.05–0.22 wt.%) as well as TiO_2 (0.01–0.16 wt.%) and MnO (~≤0.01 wt.%), whereby the latter relate to distinct mineral impurities rather than to the glauconite structure. The cross-plot of the elemental (EMP and LA-ICP-MS/MS) data and glauconite compositions, shown in Figure 3, reveals a significant overlap of the acquired chemical datasets, which demonstrates the high accuracy and robustness of both methods and analytical approaches (Figure 3c–f), confirmed by a ~80% data overlap within the 2 SD range. Accordingly, the glauconites can be classified as evolved (6–8 wt.% K_2O) to highly evolved (8–10 wt.% K_2O) and Fe-rich (≥19 wt.% TFe), with respect to the maturity definition of Odin and Matter [13]. However, small variations between the two datasets are observable, which we attribute either to the presence of sub-micron scale (both detrital and diagenetic), mineral impurities, or to sub-surface inclusions exposed and sampled during LA analysis, which are both 'invisible' to SEM and EMP techniques but can impact the LA analyses (see Figure 3a,b for documented mineral impurities and corresponding distinctive chemical trends in 3d).

The relations of the TFe, K_2O, SiO_2, and Al_2O_3 contents (Figure 3c–f) provide further insights into the glauconitization process at Langenstein. Briefly, (i) the comparatively higher Al_2O_3 and lower K_2O contents observed in sample S1 are attributable to its proximity to the transgression horizon, i.e., documenting a high detrital aluminosilicate content in the host sediment, which was subjected to glauconitization with Al being incorporated during glauconite formation and growth [62]. (ii) Progressively higher K_2O and TFe (samples S2–S5) over Al_2O_3 contents (sample S1) suggest a continuous facies shift, from continental siliciclastic (inner-shelf) to marine calcareous (mid-shelf) sedimentation, with increasing stratigraphic distance from the transgression base [29]. Finally, (iii) the linear anti-correlation between the Al_2O_3 and TFe contents in glauconite (Figure 3f) indicates that glauconite maturation proceeded through the substitution of Fe^{3+}, Fe^{2+}, and Mg^{2+} ions for Al^{3+} ions in the octahedral sites and of Al^{3+} ions for Si^{4+} ions in the tetrahedral sites, so that the resultant negative layer charge had to be balanced by the incorporation of K^+ ions and minor Na^+ and Ca^{2+} ions in the interlayer sites of glauconite [19,21,63,64].

In essence, the overall high K_2O contents in glauconite, the large overlap (i.e., homogeneity) of the glauconite compositions, and the low abundance of immature (or poorly evolved) light green grains suggest that the rate-limiting elements for glauconitization (e.g., K, Mg, Si, and Fe) were readily available at Langenstein within the specific semi-confined local micro-environments, such as fecal pellets and foraminifera chambers, and that glauconite maturation went almost to completion [13,15,21,62,65]. This mode of glauconitization is representative of modern and ancient shallow marine settings with low sedimentation rates that promote and facilitate the formation of glauconite minerals.

3.2. Mineralogical Composition and Impurities in Langenstein Glauconites

The XRD patterns obtained from the separated glauconite grains (S1–S4; note again that the green clay content in sample S5 was too small for the acquisition of the XRD pattern) reveal ordered reflections at 10 Å, 5.0 Å, 4.5 Å, 3.3 Å, 2.6 Å, and 1.51 Å (see Figure 2 in Baldermann et al. [54]), both for the glauconites from the sandstone and limestone

lithologies, which correspond to $d_{(001)}$, $d_{(002)}$, $d_{(020)}$, $d_{(003)}$, $d_{(102,13\bar{1})}$, and $d_{(060,33\bar{1})}$, respectively [13]. Additional peaks at 3.6 Å and 3.1 Å relate to $d_{(11\bar{2})}$ and $d_{(112)}$ reflections and are characteristic for the 1M polytype of glauconite, whereas the weak 'XRD bulge' between 25 and 40° 2θ belongs to minor amounts of glauconite-smectite with a $1M_d$ polytype structure [16,66]. The glauconite separates occasionally contain quartz, hydroxyl-apatite, Fe-(hydr)oxides (mainly goethite), calcite, K-feldspar, kaolinite, illite/muscovite, and illite-smectite in varying (but generally minor) amounts, which are present mainly as mineral impurities, according to BSE image data (see Figure 3a,b).

Specifically, the XRD patterns obtained from ethylene glycol-solvated, randomly oriented glauconite separates display all the glauconite reflections mentioned before as well as a weak and broad $d_{(001)}$-reflection at ~16.4 Å, which is typical for mixed-layered illite-smectite having ~60% Ilt layers and ~40% Sme layers (R1-ordered), consistent with results previously reported by Baldermann et al. [16]. Illite-smectite contributes 3 wt.% to the S1 glauconite separate, 11 wt.% in S2, and 5 wt.% in each S3 and S4, as obtained from Rietveld-based analysis of the XRD patterns (Figure 4). Minor amounts of illite/muscovite with ~95% Ilt layers and ~5% Sme layers (R3-ordered) were also identified in all glauconite separates (~2 wt.% in S1, ~1.5 wt.% in S2 and ~1 wt.% in S3–S4) based on distinct $d_{(001)}$ and $d_{(002)}$ reflections at ~9.95 Å and 4.99 Å, respectively [66].

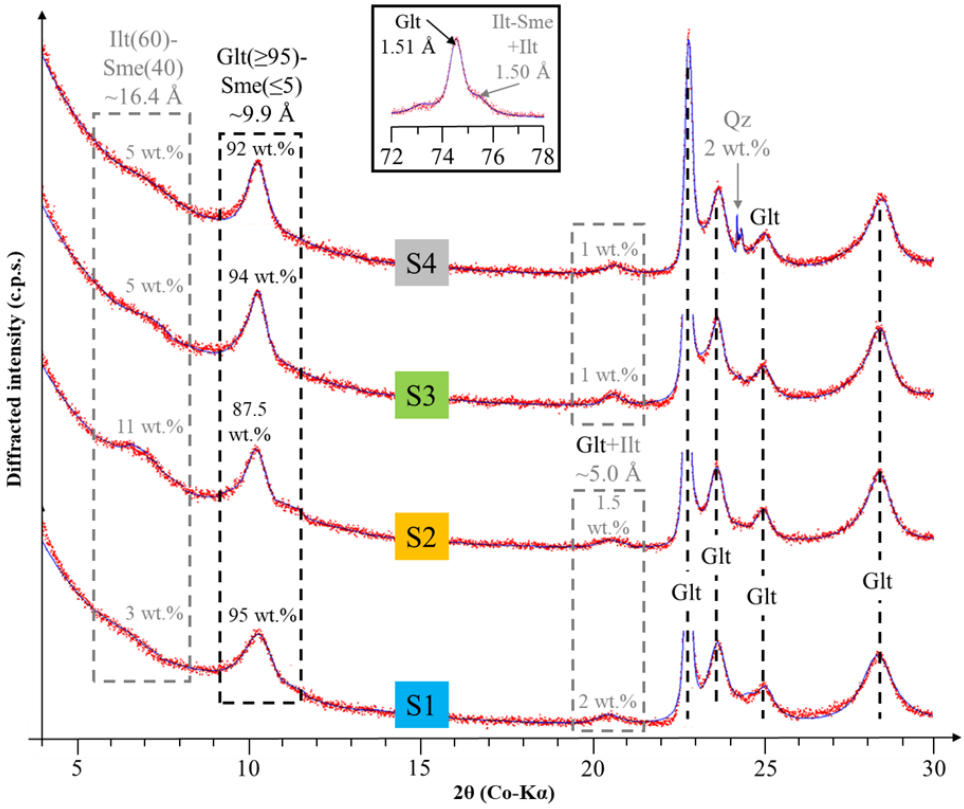

Figure 4. XRD patterns of separated glauconite powders (S1–S4) upon ethylene glycol solvation displaying characteristic peaks for glauconite (Glt-Sme), quartz (Qz), illite-smectite (Ilt-Sme), and illite/muscovite (Ilt), respectively. Red data points refer to measured diffracted intensities and blue curves mark Rietveld-based best-fitting lines.

The decreasing illite/muscovite content up-section in the profile may indicate a progressive displacement of the depositional environment, from proximal (S1) to more distal (S5) settings. Sporadically, quartz was found in sample S4, accounting for ~2 wt.% (Figure 4). All glauconites are R3-ordered, have a Glt content exceeding 95% and sum up to 87.5 to 95 wt.% of the total grain fraction. The assemblage of detrital illite/muscovite, early

diagenetic glauconite, and late diagenetic illite-smectite within single glauconite grains (Figure 3a,b) impacts the obtained Rb-Sr ages as discussed below.

3.3. Determination of Glauconite Ages via In Situ Rb-Sr Geochronology

In situ Rb-Sr dating via LA-ICP-MS/MS was carried out on glauconite separates of samples S1–S5. Approximately ~30 to 40 LA spots per sample (167 LA spots in total) were analyzed and the results are presented in Figure 5. To constrain meaningful glauconite bulk ages from the measured $^{87}Rb/^{86}Sr$ and $^{87}Sr/^{86}$ Sr ratios, an initial seawater $^{87}Sr/^{86}Sr$ value of 0.7074 for the Late Cretaceous was applied (e.g., [48]). We note here that the glauconite bulk ages most likely represent mixed ages, as inferred from XRD, EMP, and LA data showing detrital and diagenetic mineral impurities in glauconite grains (see Figures 3 and 4). Time-resolved LA measurements show overall low average Sr contents, ranging from 4.1 ppm in sample S1 to 6.5 ppm in sample S5, which along with higher Rb contents (ranging from 263.2 to 3264.8 ppm) demonstrate the applicability of the traditional Rb-Sr isochron age determination [39]. Detailed LA-ICP-MS/MS results, such as $^{87}Rb/^{86}Sr$ and $^{87}Sr/^{86}Sr$ ratios, Rb and Sr contents, and standard materials used from the GeoReM database [43], are provided in Supplementary Table S1. The isochron plots reveal glauconite bulk ages (with 1σ uncertainties shown as ellipses) of 97.34 ± 0.74 Ma for S1, 101.32 ± 0.65 Ma for S2, 97.69 ± 0.73 Ma for S3, 97.69 ± 0.78 Ma for S4, and 97.06 ± 0.88 Ma for S5, respectively (Figure 5). The MSWDs range from 0.5 to 0.9 for all samples, which indicates that the glauconite bulk ages are not overdispersed with respect to the stated analytical uncertainties [51,52].

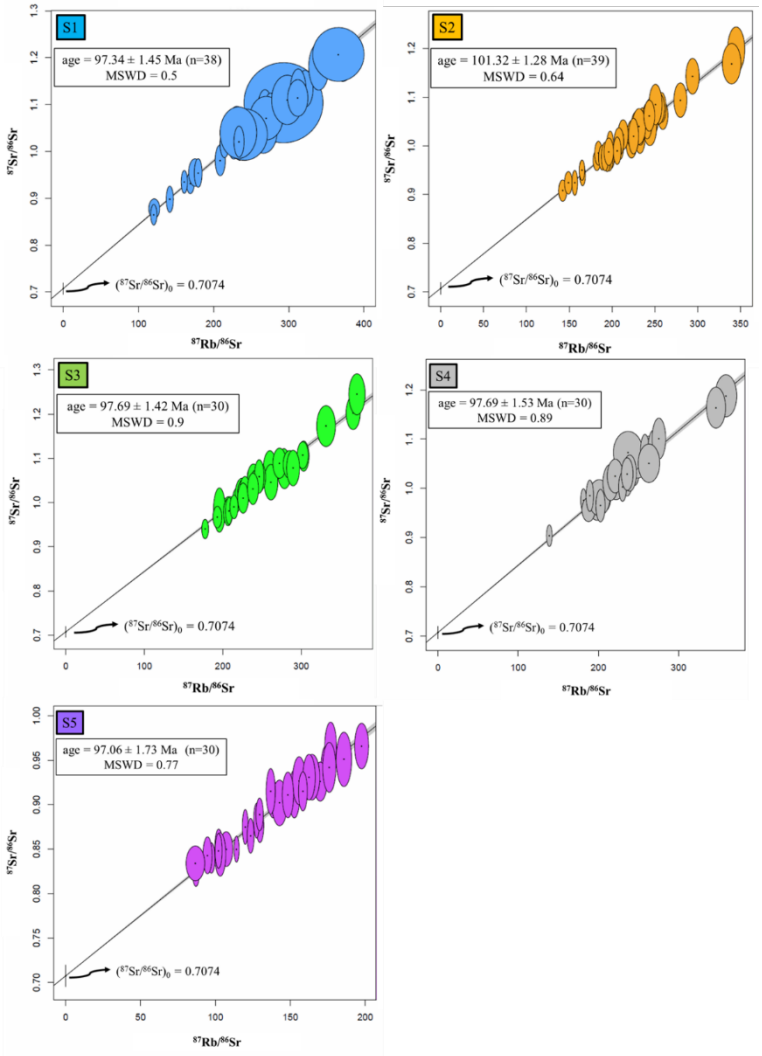

Figure 5. Isochron plots displaying glauconite bulk ages and related uncertainties (1σ is shown as ellipses and 2σ is indicated in the annotated boxes) as well as MSWD that is consistently < 1 for the glauconite separates of samples S1–S5 (n = 167). Note that an initial seawater $^{87}Sr/^{86}Sr$ value of 0.7074 for the Cretaceous was used [48].

The obtained glauconite bulk ages and their 2σ uncertainties are reasonable as (i) they generally fit within the latest Early to early Late Cretaceous, from the latest Albian to the early Middle Cenomanian (see GTS 2020), and (ii) partly overlap with published glauconite ages of 95.0 ± 1.8 Ma (K-Ar-based) reported from Langenstein for the uppermost part of the M. dixoni Zone [16]. However, a continuous geochronological progression from the transgression horizon, which is represented by the basal conglomerate and the overlying glauconite-bearing sandstone [30], toward more open marine carbonate sedimentation, represented by the Glauconitic Pläner Limestones, is barely evident from collected in situ Rb-Sr data (Figure 6). For instance, sample S1 is younger (~0.7 Ma) compared to its expected provenance from the lower M. dixoni Zone and sample S2 is comparatively older (~3 to 4 Ma) than the stratigraphic ages estimated for the Langenstein profile ([29]. Samples S3–S5, which were taken from the M. dixoni and lowermost A. rhotomagense zones, display a closer match to the estimated stratigraphic ages, as all three samples overlap within analytical uncertainty of LA-ICP-MS/MS-based dating and with expected stratigraphic ages.

From the obtained glauconite bulk ages it becomes clear that any potential post-depositional modifications and/or significant resetting of the Rb-Sr systematics of the studied glauconite are negligible. These include possible phenomena such as (i) decomposition or diagenetic dissolution of Rb- and K-rich detrital minerals (e.g., feldspar and mica) in the sediment substrate and the subsequent (ii) uptake of inherited (non-marine) Rb, K, and Sr isotope signals by authigenic or late diagenetic glauconite [67], and also (iii) a possible loss or gain of Sr during diagenetic processes or (iv) isotopic exchange with non-marine burial/diagenetic fluids [68,69]. Results also indicate that resetting of the isotopic signatures of glauconite is insignificant during comparatively shallow burial diagenesis, as is the case for the Langenstein profile (≤1500 m burial depth; ≤65 °C [16]). Overall, the presence of detrital and diagenetic mineral impurities present in single glauconite grains can have a strong impact on the measured bulk ages, which thus requires a careful petrographic screening and mineralogical characterization of the glauconites (see Figures 3 and 4). In the following section, we re-evaluate the Rb-Sr glauconite bulk ages by considering the effects of detrital (illite/muscovite) vs. diagenetic (illite-smectite) mineral impurities and contamination, which affect the age distributions measured in glauconite grains. Such micron/sub-micron-size mineral impurities are commonly 'invisible' and hard to detect visually during the LA-based Rb-Sr dating, but could be detected or quantified via XRD analysis of powdered glauconite separates.

The detrital illite/muscovite and the diagenetic illite-smectite have been previously dated to 247.2 ± 3.4 Ma (Olenekian, Early Triassic) and 68.0 ± 1.6 Ma (Maastrichtian, Late Cretaceous), respectively, based on K-Ar dating of separated grain size fractions coupled to illite polytype analysis [16]. With recognition of the distinct age distributions of the illitic phases (i.e., glauconite, illite/muscovite, and illite-smectite), which contribute to the measured Rb-Sr-based glauconite bulk ages, and their Rietveld-based mineral quantifications (Figure 3), we can deconvolve these mixed ages and calculate impurity-free, 'true' glauconite ages, according to the equation:

$$Age_{Glt}\ (Ma) = Bulk\ age_{Glt}\ (Ma) - \%Ilt\text{-}Sme \times Age_{Ilt\text{-}Sme}\ (Ma) + \%Ilt/Ms \times Age_{Ilt/Ms}\ (Ma)$$

where %Ilt-Sme and %Ilt/Ms are the fractions (in wt.%) of illite-smectite and illite/muscovite phases in the bulk glauconite separates, bulk age_{Glt} is the Rb-Sr-based glauconite bulk age, which includes the aforementioned mineral impurities; and $age_{Ilt\text{-}Sme}$ and $age_{Ilt/Ms}$ are the depositional ages of illite-smectite and illite/muscovite determined by K-Ar dating [16]. Detailed information is available in Supplementary Table S3.

The calculations assume that the provenance and hence the age of the detrital illitic phases did not change through the transgression. We further note that a classical error propagation analysis is barely possible, given that the uncertainty of the XRD quantifications is poorly constrained. However, if we apply the known uncertainties of the Rb-Sr and K-Ar ages obtained for each illitic phase to the calculated illitic fractions present in each sample S1–S5 (and taking these estimates as absolute), the uncertainty of the corrected glauconite ages is only ~0.1 to 0.2% relative to the glauconite bulk ages, because these mineral impurities account for only a minor proportion of the total glauconite grains. If we, however, consider a ± 3 wt.% uncertainty to the calculated illitic fractions [70], then the uncertainty of the corrected glauconite ages increases to 0.4–11% relative to the glauconite bulk ages, which is much larger than the estimated duration of the entire Langenstein section. In the following, we thus present the corrected glauconite ages relative to the bio-stratigraphic position in the Langenstein profile without providing explicit uncertainties to each sample.

Sample S1 contains 3 wt.% illite-smectite, 2 wt.% illite/muscovite, and 95 wt.% glauconite and has a mixed age of 97.34 ± 1.45 Ma, which gives a corrected glauconite age of ~100.2 Ma, which corresponds to the lowermost M. mantelli Zone. This unexpected finding might be an indication of a hitherto not identified first transgression event in the earliest Cenomanian, corresponding to the ultimus/Aucellina Transgression in the regional literature (e.g., [29,71]). This observation may corroborate the early records of *Ammonites mantelli* from Langenstein [31,72]. By contrast, sample S2 is characterized by a higher illite-smectite content (11 wt.%), a similar illite/muscovite content (1.5 wt.%), and a smaller glauconite content (86.5 wt.%), and it has a mixed age of 101.32 ± 1.28 Ma, resulting in a corrected glauconite age of ~97.5 Ma, thus transferring it into the expected position within the M. dixoni Zone. Similar data processing yields corrected glauconite ages of ~96.8 Ma for samples S3 and S4, corresponding to the upper part of the M. dixoni Zone from where the two samples were obtained. Sample S5 is assumed to have a more equal clay mineral assemblage than S3 and S4, based on an alike geochemical composition (Figure 3) and identical facies association (Figure 2), resulting in a corrected glauconite age of ~96.1 Ma, which fits well to the expected age within the lower A. rhotomagense Zone (Figure 6). The deconvoluted glauconite ages and their close relation to the biostratigraphy of the Langenstein profile (Figure 6) allow us to further draw conclusions about the rate of the shallow-water glauconitization process at this paleo-site.

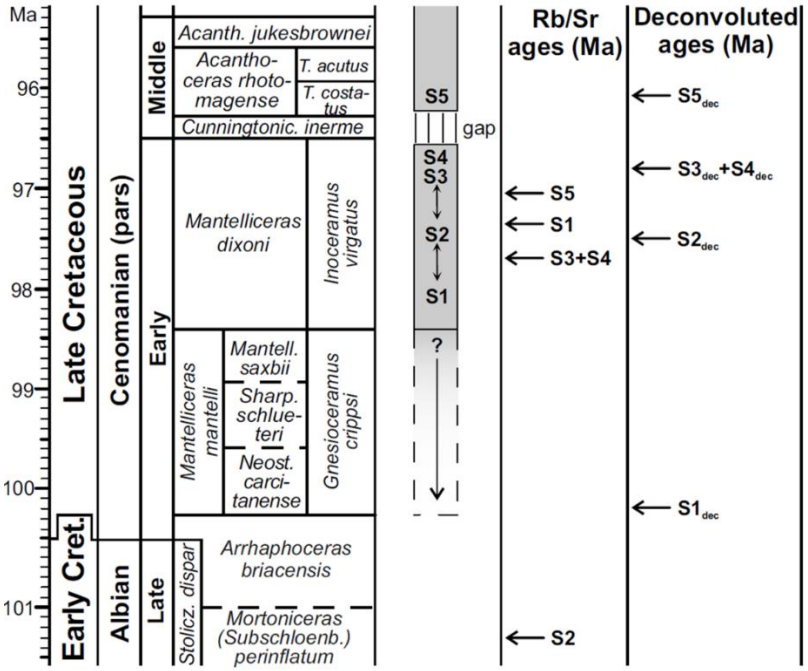

Figure 6. Bio-stratigraphic and geochronologic framework of the Langenstein section and absolute ages of samples S1–S5. The bio-stratigraphic position of the Langenstein section is based on Horna [16] and Wilmsen [29], starting in the late Early Cenomanian M. dixoni Zone (grey bar), with approximate positions of samples used in this study (note the stratigraphic gap in the Early–Middle Cenomanian boundary interval). The light-grey range bar with broken line indicates a potential downward extension of the section into the earliest Cenomanian, corroborated by the corrected age of sample S1. The measured Rb-Sr ages of samples S1–S5 generally overlap with the expected bio-stratigraphic age within analytical uncertainty (except for sample S2) but show no consistent stratigraphic age progression. The deconvoluted ages of samples S1–S5 are in stratigraphic order and fall within the expected M. dixoni and A. rhotomagense zones (note the outlier of sample S1 that suggests the presence of the lower M. mantelli Zone in the lowermost part of the Langenstein section, potentially reflecting an earlier Cenomanian transgression event). Absolute ages are after GTS 2020 [73] and cyclo-stratigraphic considerations; ammonite biostratigraphy is after Wright and Kennedy [28]).

3.4. Timing of Glauconite Formation

It has been proposed that the characteristics of the host lithology (e.g., nature and resistance to alteration of the sediment substrate and its porosity, permeability, tortuosity, and organic matter content), as well as physicochemical and environmental controls (e.g., pH, T, redox conditions, and fluid chemistry), affect the chemical and mineralogical composition of glauconite minerals during their progressive evolution from Fe-smectite to glauconite end-members at the seawater–sediment interface [14,15,17,65,74]. In recent years, the influences of chemical and isotopic (dis-)equilibrium between detrital siliciclastic vs. calcareous substrates, seawater, and pore fluids on glauconitization pathways have been relatively well-constrained, yet the rate of glauconite formation remains disputed.

In deep-water settings, glauconite formation is believed to be extremely slow, requiring up to ~9 Ma to form >90%Glt layers in Glt-Smc [70], which is mainly due to the low temperature (<5 °C) of the deep ocean waters and the limited or discontinuous supply of the rate-limiting elements, such as Fe [22]. The glauconite grains forming in such cold environments are often characterized by a heterogenous composition [75] and may show a large variability in formation ages, reflecting slower sedimentation rates and related decreased influx of reactive chemical components needed for glauconitization or interrupted elemental diffusion paths within the micro-environment, thus leaving immature glauconite or glauconite-smectite in the sedimentary rock record (scenario 2 in Figure 1). By contrast, mature glauconite grains with a homogenous chemical composition and comparatively small age variation may form in shallow-water settings of the present-day and ancient oceans, which is due to an enhanced influx of more reactive terrigenous components [76,77], warmer temperatures (~10 to 20 °C [78]) and increased primary production (organic carbon [79]), promoting mineral dissolution and redox reactions [80] that continuously supply key elements needed for glauconite formation and maturation. Under such conditions, glauconitization is proposed to proceed faster, taking only ~1 Ma to complete at the sediment–seawater interface during early diagenesis (scenario 1 in Figure 1 [65]).

However, analytical challenges of glauconite dating, such as the incorporation of inherited non-marine and typically more radiogenic Sr due to substrate interaction [81], presence of detrital Rb- and K-bearing feldspars and mica within glauconite grains [67], post-depositional alteration into Fe-illite or nontronite [69], and subsequent post-depositional resetting of the glauconite Rb-Sr isotope system [82,83], have until now prevented a good assessment of glauconitization rates for deep-water and shallow-marine settings.

Meunier and El Albani [22] argue that the plot of glauconite compositions in the $M^+/4Si$ vs. Fe/sum of octahedral cations diagram provides insights into the rate of chemical diffusion in sediments, bulk sedimentation, rates, and corresponding glauconitization rates, whereby higher M^+ (i.e., K^+, Na^+, and Ca^{2+}) and TFe contents indicate slow glauconite formation associated with low sedimentation rates, while higher Al^{3+} and lower K^+ contents suggest fast glauconite precipitation at higher sedimentation rates (Figure 7). This plot implies slowly progressing and diffusion-controlled glauconitization for the

Langenstein glauconites, (Figure 7), which is not consistent with our obtained glauconite ages (Figure 6) and their high maturity (Figure 3). This may suggest that mechanisms and environmental controls other than sedimentation rate must be considered to explain fast progressing glauconitization in warm, shelfal sequences.

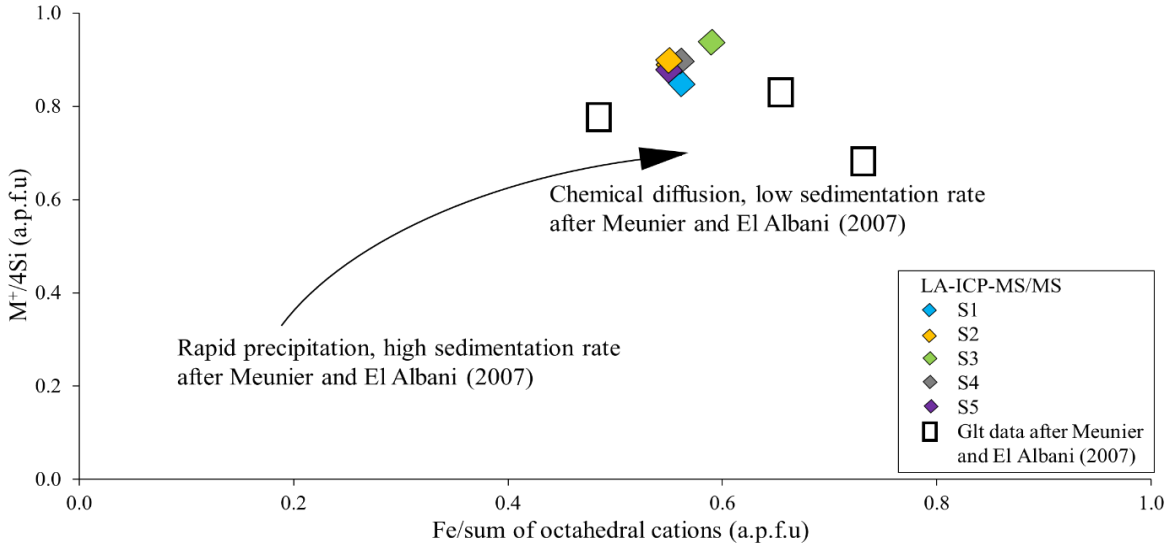

Figure 7. Plot of the average glauconite compositions obtained by LA-ICP-MS/MS analysis in the $M^+/4Si$ vs. Fe/sum of octahedral cations diagram [22]. Slowly progressing glauconite formation is indicated, which is inconsistent with our glauconite ages measured by in situ Rb-Sr dating of glauconite grain separates.

The Langenstein glauconites are highly evolved, well-preserved, and have been formed soon after sediment deposition (i.e., ~0.1 to ~1 Ma; average: ~0.3 ± 0.5 Ma), as determined by the difference in the bio-stratigraphic and corrected glauconite age (see Figure 6), which calls for fast glauconitization immediately at the sediment–seawater interface and continuous supply of key elements, such as K, Mg, Al, Si, and Fe [19]. Recently, Wilmsen and Bansal [23] have basically drawn the same conclusion based on a study of Cenomanian glauconites from the Elbtal Group (Saxony, eastern Germany), which formed within ≤0.4 Ma in a nearshore siliciclastic depositional system. They argue that glauconite formation occurred under warm conditions on rather short time scales and under, in part, high accumulation rates and thus under environmental conditions fundamentally different from recent ones. From oxygen isotopic signatures of the calcareous substrate, a formation temperature of 26 ± 2 °C has been reported for the Langenstein sequence [54], which is typical for warm shelfal settings of the Cretaceous. Such rapidly forming glauconites can indeed represent a reliable and robust mineral archive, which is applicable for geochronological age dating, paleo-reconstructions, and regional correlation of localities.

It is generally accepted that a few thousands of years are needed to precipitate sufficient amounts of Fe-smectite [84], which subsequently matures to glauconite on different timescales, which may range from ~5 to > 10 Ma for cold, deep-water settings to <1 Ma for warm, shallow-water areas (Figure 8). Our mineralogical and geochronological characterization of the glauconites from Langenstein suggests that ~100% glauconitization (i.e., complete transformation of %Sme layers into %Glt layers in glauconite grains; expressed as the degree of glauconitization in Figure 8) was reached within ~0.4 Ma, documenting another example of fast glauconite formation and maturation, as described in scenario 1 (Figure 1). A comparison of the glauconite formation rate obtained in this study with present-day rates in shallow- vs. deep-seas reveals that during the Late Cretaceous the glauconitization process was much faster (Figure 8).

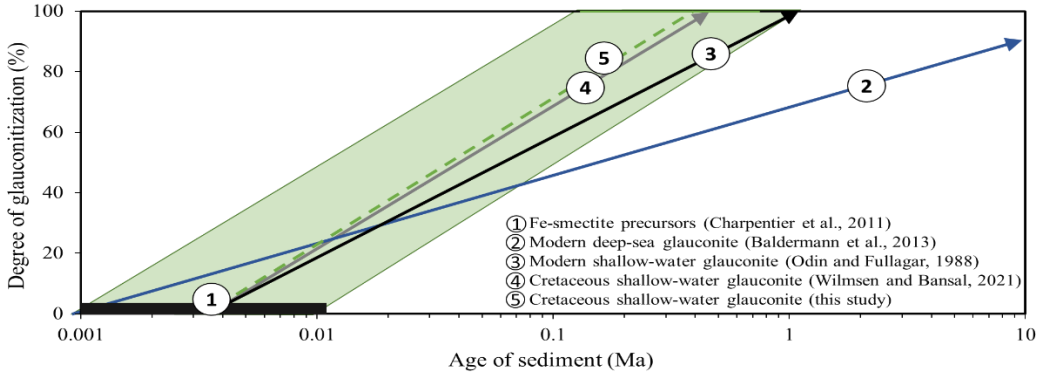

Figure 8. Comparison of glauconite formation rates for the Langenstein shelfal setting (early Late Cretaceous) with present-day and Late Cretaceous shallow-water and deep-sea environments. The proposed glauconitization rate for Langenstein generally follows the modern shallow-water glauconitization path, but is faster probably due to Cretaceous 'greenhouse' conditions, which could have triggered continental-chemical weathering rates and thus increased inputs of key elements (K, Mg, Si, Al, and Fe) into the oceans needed for rapid glauconite formation.

We attribute the rapid glauconitization at Langenstein to warm 'greenhouse' conditions with a general sea-level highstand in the Cretaceous [85] coupled with intense continental weathering, which resulted in high inputs of solid and dissolved terrestrially derived elements into the oceans [86]. By contrast, in modern settings, glauconite formation is slower due to a general sea-level lowstand and cooler 'icehouse' conditions. This accelerated mode of glauconite formation may have occurred in shallow seas worldwide over much of the Phanerozoic and especially during times of global 'greenhouses' coupled with increased chemical weathering fluxes, which is also supported by recently described and quantified elemental sequestration trends associated with green clay authigenesis in marine sediments through time [55].

4. Conclusions

We have studied the timing and the formation conditions of authigenic glauconite within the early Late Cretaceous shelfal sequence from Langenstein (northern Germany) using combined petrographical-chemical (EMP) and mineralogical (XRD) screening methods and in situ Rb-Sr dating of glauconite grains via LA-ICP-MS/MS. We demonstrate that suitable glauconite grains can provide a directly datable, widespread, and robust mineral archive for paleo-environmental and geochronological studies if glauconite formation ages affected by later diagenetic and/or detrital mineral impurities (illite, feldspar, etc.) can be accounted for and deconvoluted. The following conclusions can be drawn:

(1) Almost pure (i.e., impurity-free) and highly evolved glauconites, which record meaningful stratigraphic ages, can be identified, and precisely dated via a combination of K-Ar and Rb-Sr dating and careful mineralogical and petrographic screening of glauconite grains.

(2) The herein corrected Rb-Sr ages at the equivalent stratigraphic position are consistent with previously published K-Ar ages (95 ± 1.8 Ma [16]), arguing for low uncertainties and thus provide confidence in the Rb-Sr results.

(3) Exposure of glauconite grains to shallow burial diagenesis (T ≤ 65 °C, 1500 m burial depth) has no measurable effect on pristine Rb-Sr systematics of glauconite and thus its ages, which calls for a reappraisal of glauconite geochronology applications in Earth sciences.

(4) Comparison of glauconite ages vs. sediment depositional ages for the Langenstein profile suggests fast glauconitization within <1 Ma, which we relate to Cretaceous greenhouse climate with high atmospheric CO_2 levels and elevated chemical weathering fluxes to the oceans.

(5) Shallow-water glauconitization in the Late Cretaceous was much faster compared to modern rates of glauconite formation in shallow- vs. deep-sea environments, which we relate to unique Cretaceous seawater chemistry.

(6) Future studies should (i) explore the robustness of the glauconite isotopic signatures for paleo-seawater and environmental reconstructions, (ii) assess the degree of preservation of glauconite ages in other deposits (deep-sea), (iii) test if the herein presented age deconvolution and mineral screening approaches are applicable to other glauconite-bearing deposits, and (iii) study the impact of distinct diagenetic/burial (higher T) conditions on glauconite ages.

Supplementary Materials: The following supporting information can be downloaded at: www.mdpi.com/article/10.3390/min12070818/s1, Figure S1: Backscatter electron image showing mineral inclusions within a glauconite grain determined by electron microprobe (EMP) analysis. The chemical composition of the highlighted areas and points are given in the table below.; Table S1: Compilation of $^{87}Rb/^{86}Sr$ and $^{87}Sr/^{86}Sr$ ratios with corresponding uncertainties (2σ) for both reference materials and glauconites determined by LA-ICP-MS/MS. NIST610 was used as primary reference material; BCR2G was used as secondary reference material. Rb and Sr concentrations (ppm) are reported only for the Langenstein glauconites.; Table S2: Chemical composition (in wt.%) of glauconite grains (S1–S5) sampled from the Langenstein profile obtained by LA-ICP-MS/MS analyses.; Table S3: Comparison of stratigraphic ages, bulk glauconite depositional ages, and deconvoluted glauconite depositional ages of samples taken from five glauconite-bearing intervals from the Langenstein profile. The mineralogical composition of the glauconite grains was determined by X-ray diffraction analyses. Rb-Sr data were collected by LA-ICP-MS/MS.

Author Contributions: Investigation and methodology, data curation, formal analysis: E.S., U.M., S.L., M.W., J.F., D.G., A.M.B., T.Z., and A.B.; conceptualization and project administration: A.B. All authors contributed to the writing of the original draft. All authors have read and agreed to the published version of the manuscript.

Funding: Open Access Funding by the Graz University of Technology. This research was funded by the ARC Discovery Project (DP210100462; grant to J.F., S.L., A.B., and T.Z.) titled "Glauconite: Archive recording the timing and triggers of Cambrian radiation".

Data Availability Statement: The data generated in this study are provided in the Supplementary Material. The studied geological samples from the Langenstein section are archived in the mineral collection of the Institute of Applied Geosciences (Graz University of Technology) and can be made available upon request to A.B. All samples were collected and exported in a responsible manner, and in accordance with relevant permits and local laws.

Acknowledgments: This work was supported via the NAWI Graz Geocenter (TU Graz) and by TU Graz Open Access Publishing Fund. We kindly acknowledge Cyrill Grengg (TU Graz) for assistance with the electron microprobe analysis.

Conflicts of Interest: The authors declare no conflicts of interest.

References

1. Du Vivier, A.; Selby, D.; Condon, D.; Takashima, R.; Nishi, H. Pacific $^{187}Os/^{188}Os$ isotope chemistry and U–Pb geochronology: Synchroneity of global Os isotope change across OAE 2. *Earth Planet. Sci. Lett.* **2015**, *428*, 204–216. https://doi.org/10.1016/j.epsl.2015.07.020.
2. Griffis, N.P.; Mundil, R.; Montañez, I.P.; Isbell, J.; Fedorchuk, N.; Vesely, F.; Iannuzzi, R.; Yin, Q.-Z. A new stratigraphic framework built on U-Pb single-zircon TIMS ages and implications for the timing of the penultimate icehouse (Paraná Basin, Brazil). *GSA Bull.* **2018**, *130*, 848–858. https://doi.org/10.1130/b31775.1.
3. Du, X.; Lu, Y.; Duan, D.; Liu, Z.; Zhao, K.; Jia, J.; Fu, H. Was volcanic activity during the Ordovician-Silurian transition in South China part of a global phenomenon? Constraints from zircon U–Pb dating of volcanic ash beds in black shales. *Mar. Pet. Geol.* **2020**, *114*, 104209.
4. Lúcio, T.; Neto, J.A.S.; Selby, D. Late Barremian/Early Aptian Re–Os age of the Ipubi Formation black shales: Stratigraphic and paleoenvironmental implications for Araripe Basin, northeastern Brazil. *J. S. Am. Earth Sci.* **2020**, *102*, 102699.
5. Huff, W.D.; Bergström, S.M.; Kolata, D.R. Gigantic Ordovician volcanic ash fall in North America and Europe: Biological, tectonomagmatic, and event-stratigraphic significance. *Geology* **1992**, *20*, 875–878.

6. Zhao, T.; Algeo, T.J.; Feng, Q.; Zi, J.-W.; Xu, G. Tracing the provenance of volcanic ash in Permian–Triassic boundary strata, South China: Constraints from inherited and syn-depositional magmatic zircons. *Palaeogeogr. Palaeoclimatol. Palaeoecol.* **2019**, *516*, 190–202.
7. Halverson, G.; Hoffman, P.F.; Schrag, D.P.; Maloof, A.C.; Rice, A.H.N. Toward a Neoproterozoic composite carbon-isotope record. *GSA Bull.* **2005**, *117*, 1181. https://doi.org/10.1130/b25630.1.
8. Partin, C.; Bekker, A.; Planavsky, N.; Scott, C.; Gill, B.; Li, C.; Podkovyrov, V.; Maslov, A.; Konhauser, K.; Lalonde, S.; et al. Large-scale fluctuations in Precambrian atmospheric and oceanic oxygen levels from the record of U in shales. *Earth Planet. Sci. Lett.* **2013**, *369–370*, 284–293. https://doi.org/10.1016/j.epsl.2013.03.031.
9. Straeten, C.A.V. K-bentonites, volcanic ash preservation, and implications for Early to Middle Devonian volcanism in the Acadian orogen, eastern North America. *Geol. Soc. Am. Bull.* **2004**, *116*, 474–489.
10. Baldermann, A.; Mittermayr, F.; Bernasconi, S.M.; Dietzel, M.; Grengg, C.; Hippler, D.; Boch, R. Fracture dolomite as an archive of continental palaeo-environmental conditions. *Commun. Earth Environ.* **2020**, *1*, 35.
11. Mavromatis, V.; van Zuilen, K.; Purgstaller, B.; Baldermann, A.; Nägler, T.F.; Dietzel, M. Barium isotope fractionation during witherite ($BaCO_3$) dissolution, precipitation and at equilibrium. *Geochim. Cosmochim. Acta* **2016**, *190*, 72–84. https://doi.org/10.1016/j.gca.2016.06.024.
12. Purgstaller, B.; Dietzel, M.; Baldermann, A.; Mavromatis, V. Control of temperature and aqueous Mg^{2+}/Ca^{2+} ratio on the (trans-) formation of ikaite. *Geochim. Cosmochim. Acta* **2017**, *217*, 128–143.
13. Odin, G.S.; Matter, A. De glauconiarum origine. *Sedimentology* **1981**, *28*, 611–641. https://doi.org/10.1111/j.1365-3091.1981.tb01925.x.
14. Amorosi, A. Chromium and nickel as indicators of source-to-sink sediment transfer in a Holocene alluvial and coastal system (Po Plain, Italy). *Sediment. Geol.* **2012**, *280*, 260–269. https://doi.org/10.1016/j.sedgeo.2012.04.011.
15. Banerjee, S.; Bansal, U.; Thorat, A.V. A review on palaeogeographic implications and temporal variation in glaucony composition. *J. Palaeogeogr.* **2016**, *5*, 43–71. https://doi.org/10.1016/j.jop.2015.12.001.
16. Baldermann, A.; Dietzel, M.; Mavromatis, V.; Mittermayr, F.; Warr, L.N.; Wemmer, K. The role of Fe on the formation and diagenesis of interstratified glauconite-smectite and illite-smectite: A case study of Upper Cretaceous shallow-water carbonates. *Chem. Geol.* **2017**, *453*, 21–34. https://doi.org/10.1016/j.chemgeo.2017.02.008.
17. López-Quirós, A.; Escutia, C.; Sánchez-Navas, A.; Nieto, F.; Garcia-Casco, A.; Martín-Algarra, A.; Evangelinos, D.; Salabarnada, A. Glaucony authigenesis, maturity and alteration in the Weddell Sea: An indicator of paleoenvironmental conditions before the onset of Antarctic glaciation. *Sci. Rep.* **2019**, *9*, 13580. https://doi.org/10.1038/s41598-019-50107-1.
18. Choudhury, T.R.; Banerjee, S.; Khanolkar, S.; Saraswati, P.K.; Meena, S.S. Glauconite authigenesis during the onset of the Paleocene-Eocene Thermal Maximum: A case study from the Khuiala Formation in Jaisalmer Basin, India. *Palaeogeogr. Palaeoclim. Palaeoecol.* **2021**, *571*, 110388. https://doi.org/10.1016/j.palaeo.2021.110388.
19. Fernández-Landero, S.; Fernández-Caliani, J. Mineralogical and Crystal-Chemical Constraints on the Glauconite-Forming Process in Neogene Sediments of the Lower Guadalquivir Basin (SW Spain). *Minerals* **2021**, *11*, 578. https://doi.org/10.3390/min11060578.
20. Tribovillard, N.; Bout-Roumazeilles, V.; Delattre, M.; Ventalon, S.; Abraham, R.; Nzié, O. Syndepositional glauconite as a paleoenvironmental proxy—The lower Cenomanian Chalk of Cap Blanc Nez (N-France). *Chem. Geol.* **2021**, *584*, 120508. https://doi.org/10.1016/j.chemgeo.2021.120508.
21. Amorosi, A.; Sammartino, I.; Tateo, F. Evolution patterns of glaucony maturity: A mineralogical and geochemical approach. *Deep Sea Res. Part II Top. Stud. Oceanogr.* **2007**, *54*, 1364–1374. https://doi.org/10.1016/j.dsr2.2007.04.006.
22. Meunier, A.; El Albani, A. The glauconite–Fe-illite–Fe-smectite problem: A critical review. *Terra Nova* **2007**, *19*, 95–104.
23. Wilmsen, M.; Bansal, U. Depositional setting and limiting factors of early Late Cretaceous glaucony formation: Implications from Cenomanian glauconitic strata (Elbtal Group, Germany). *Facies* **2021**, *67*, 24. https://doi.org/10.1007/s10347-021-00627-y.
24. Clauer, N.; Keppens, E.; Stille, P. Sr isotopic constraints on the process of glauconitization. *Geology* **1992**, *20*, 133–136. https://doi.org/10.1130/0091-7613(1992)020<0133:sicotp>2.3.co;2.
25. Morton, J.P.; Long, L.E. Rb-Sr dating of Paleozoic glauconite from the Llano region, central Texas. *Geochim. et Cosmochim. Acta* **1980**, *44*, 663–672. https://doi.org/10.1016/0016-7037(80)90156-8.
26. Obradovich, J.D. A different perspective on glauconite as a chronometer for geologic time scale studies. *Paleoceanography* **1988**, *3*, 757–770. https://doi.org/10.1029/pa003i006p00757.
27. Selby, E.A.; Joiner, T.E., Jr. Cascades of emotion: The emergence of borderline personality disorder from emotional and behavioral dysregulation. *Rev. Gen. Psychol.* **2009**, *13*, 219–229.
28. Wright, C.W.; Kennedy, W.J. The Ammonoidea of the Lower Chalk. Part 7. *Palaeontogr. Soc. Monogr.* **2017**, *648*, 461–561.
29. Wilmsen, M. Sequence stratigraphy and palaeoceanography of the Cenomanian Stage in northern Germany. *Cretac. Res.* **2003**, *24*, 525–568. https://doi.org/10.1016/s0195-6671(03)00069-7.
30. Wilmsen, M.; Niebuhr, B.; Hiss, M. The Cenomanian of northern Germany: Facies analysis of a transgressive biosedimentary system. *Facies* **2005**, *51*, 242–263. https://doi.org/10.1007/s10347-005-0058-5.
31. Horna, F. Die Cenomantransgression von Langenstein: Alter und eventstratigraphische position. *Neues Jahrb. Geol. Und Paläontol.-Abh.* **1997**, *203*, 47–56.

32. Voigt, T.; von Eynatten, H. Das Subherzyne Kreidebecken. In *Exkursionsführer: Die Kreide des Subherzynen und Östlichen Niedersächsischen Beckens*; Mutterlose, J., Steffahn, J., Eds.; 2004; Bochumer Geologische und Geotechnische Arbeiten: Bochum, Germany, 2004; Volume 4, p. 54.
33. Voigt, T.; Wiese, F.; von Eynatten, H.; Franzke, H.-J.; Gaupp, R. Facies evolution of syntectonic Upper Cretaceous deposits in the Subhercynian Cretaceous Basin and adjoining areas (Germany). *Z.-Dtsch. Ges. Geowiss.* **2006**, *157*, 203–244.
34. Baldermann, A.; Kaufhold, S.; Dohrmann, R.; Baldermann, C.; Letofsky-Papst, I.; Dietzel, M. A novel nZVI–bentonite nanocomposite to remove trichloroethene (TCE) from solution. *Chemosphere* **2021**, *282*, 131018. https://doi.org/10.1016/j.chemosphere.2021.131018.
35. Bandura, D.R.; Baranov, V.I.; Tanner, S.D. Reaction chemistry and collisional processes in multipole devices for resolving isobaric interferences in ICP-MS. *Anal. Bioanal. Chem.* **2001**, *370*, 454–470. https://doi.org/10.1007/s002160100869.
36. Cheng, P.; Koyanagi, G.K.; Bohme, D.K. On the chemical resolution of the 87Rb+ (s0)/87Sr+ (s1) isobaric interference: A kinetic search for an optimum reagent. *Anal. Chim. Acta* **2008**, *627*, 148–153.
37. Hogmalm, K.J.; Zack, T.; Karlsson AK, O.; Sjöqvist, A.S.; Garbe-Schönberg, D. In situ Rb–Sr and K–Ca dating by LA-ICP-MS/MS: An evaluation of N_2O and SF_6 as reaction gases. *J. Anal. At. Spectrom.* **2017**, *32*, 305–313.
38. Zack, T.; Hogmalm, K.J. Laser ablation Rb/Sr dating by online chemical separation of Rb and Sr in an oxygen-filled reaction cell. *Chem. Geol.* **2016**, *437*, 120–133.
39. Tillberg, M.; Drake, H.; Zack, T.; Kooijman, E.; Whitehouse, M.J.; Åström, M.E. In situ Rb-Sr dating of slickenfibres in deep crystalline basement faults. *Sci. Rep.* **2020**, *10*, 562.
40. Govindaraju, K.; Roelandts, I. Compilation report (1966–1987) on trace elements in five CRPG geochemical reference samples: Basalt BR; Granites, GA and GH; Micas, Biotite Mica-Fe and Phlogopite Mica-Mg. *Geostand. Newsl.* **1988**, *12*, 119–201.
41. Woodhead, J.; Hergt, J.M. Strontium, Neodymium and Lead Isotope Analyses of NIST Glass Certified Reference Materials: SRM 610, 612, 614. *Geostand. Geoanalytical Res.* **2001**, *25*, 261–266. https://doi.org/10.1111/j.1751-908x.2001.tb00601.x.
42. Elburg, M.; Vroon, P.; van der Wagt, B.; Tchalikian, A. Sr and Pb isotopic composition of five USGS glasses (BHVO-2G, BIR-1G, BCR-2G, TB-1G, NKT-1G). *Chem. Geol.* **2005**, *223*, 196–207. https://doi.org/10.1016/j.chemgeo.2005.07.001.
43. Jochum, K.P.; Nohl, U.; Herwig, K.; Lammel, E.; Stoll, B.; Hofmann, A.W. GeoReM: A New Geochemical Database for Reference Materials and Isotopic Standards. *Geostand. Geoanal. Res.* **2005**, *29*, 333–338. https://doi.org/10.1111/j.1751-908x.2005.tb00904.x.
44. Charlier, B.; Ginibre, C.; Morgan, D.; Nowell, G.; Pearson, D.; Davidson, J.; Ottley, C. Methods for the microsampling and high-precision analysis of strontium and rubidium isotopes at single crystal scale for petrological and geochronological applications. *Chem. Geol.* **2006**, *232*, 114–133. https://doi.org/10.1016/j.chemgeo.2006.02.015.
45. Wise, S.A.; Watters, R.L. *Certificate of Analysis: Standard Reference Material 610*; National Institute of Standards and Technology: Gaithersburg, MD, USA, 2012.
46. Redaa, A.; Farkaš, J.; Gilbert, S.; Collins, A.S.; Wade, B.; Löhr, S.; Zack, T.; Garbe-Schönberg, D. Assessment of elemental fractionation and matrix effects during in situ Rb–Sr dating of phlogopite by LA-ICP-MS/MS: Implications for the accuracy and precision of mineral ages. *J. Anal. At. Spectrom.* **2020**, *36*, 322–344. https://doi.org/10.1039/d0ja00299b.
47. Paton, C.; Hellstrom, J.; Paul, B.; Woodhead, J.; Hergt, J. Iolite: Freeware for the visualisation and processing of mass spectrometric data. *J. Anal. At. Spectrom.* **2011**, *26*, 2508–2518. https://doi.org/10.1039/c1ja10172b.
48. Veizer, J.; Ala, D.; Azmy, K.; Bruckschen, P.; Buhl, D.; Bruhn, F.; Carden GA, F.; Diener, A.; Ebneth, S.; Godderis, Y.; et al. 87Sr/86Sr, δ13C and δ18O evolution of Phanerozoic seawater. *Chem. Geol.* **1999**, *161*, 59–88.
49. Rösel, D.; Zack, T. LA-ICP-MS/MS Single-Spot Rb-Sr Dating. *Geostand. Geoanal. Res.* **2022**, *46*, 143–168.
50. Vermeesch, P. IsoplotR: A free and open toolbox for geochronology. *Geosci. Front.* **2018**, *9*, 1479–1493. https://doi.org/10.1016/j.gsf.2018.04.001.
51. Nicolaysen, L.O. Graphic interpretaion of discordant age measurements on metamorphic rocks. *Ann. N. Y. Acad. Sci.* **1961**, *91*, 198–206.
52. York, D.; Evensen, N.M.; Martínez, M.L.; Delgado, J.D.B. Unified equations for the slope, intercept, and standard errors of the best straight line. *Am. J. Phys.* **2004**, *72*, 367–375. https://doi.org/10.1119/1.1632486.
53. Villa, I.; De Bièvre, P.; Holden, N.; Renne, P. IUPAC-IUGS recommendation on the half life of 87Rb. *Geochim. Cosmochim. Acta* **2015**, *164*, 382–385. https://doi.org/10.1016/j.gca.2015.05.025.
54. Longerich, H.P.; Jackson, S.E.; Günther, D. Inter-laboratory note. Laser ablation inductively coupled plasma mass spectrometric transient signal data acquisition and analyte concentration calculation. *J. Anal. At. Spectrom.* **1996**, *11*, 899–904. https://doi.org/10.1039/ja9961100899.
55. Baldermann, A.; Banerjee, S.; Czuppon, G.; Dietzel, M.; Farkaš, J.; Löhr, S.; Moser, U.; Scheiblhofer, E.; Wright, N.M.; Zack, T. Impact of green clay authigenesis on element sequestration in marine settings. *Nat. Commun.* **2022**, *13*, 1527. https://doi.org/10.1038/s41467-022-29223-6.
56. Odin, G.S. (Ed.). *Green Marine Clays: Oolitic Ironstone Facies, Verdine Facies, Glaucony Facies and Celadonite-Bearing Rock Facies—A Comparative Study*; Elsevier: Amsterdam, The Netherlands, 1988; Volume 45, pp. 221–295.
57. Deb, S.P.; Fukuoka, M. Fe-Illites in A Proterozoic Deep Marine Slope Deposit in the Penganga Group of the Pranhita Godavari Valley: Their Origin and Environmental Significance. *J. Geol.* **1998**, *106*, 741–750. https://doi.org/10.1086/516057.
58. Bandopadhyay, P.C. Interpretation of authigenic vs. allogenic green peloids of ferric clay in the Proterozoic Penganga Group, southern India. *Clay Miner.* **2007**, *42*, 471–485. https://doi.org/10.1180/claymin.2007.042.4.06.

59. Eder, V.G.; Martìn-Algarra, A.; Sánchez-Navas, A.; Zanin, Y.N.; Zamirailova, A.G.; Lebedev, Y.N. Depositional controls on glaucony texture and composition, Upper Jurassic, West Siberian Basin. *Sedimentology* **2007**, *54*, 1365–1387.
60. Navas, A.S.; Algarra, A.M.; Eder, V.; Reddy, B.J.; Nieto, F.; Zanin, Y.N. Color, mineralogy and composition of upper jurassic west siberian glauconite: Useful indicators of paleoenvironment. *Can. Miner.* **2008**, *46*, 1249–1268. https://doi.org/10.3749/canmin.46.5.1249.
61. Rafiei, M.; Löhr, S.; Baldermann, A.; Webster, R.; Kong, C. Quantitative petrographic differentiation of detrital vs diagenetic clay minerals in marine sedimentary sequences: Implications for the rise of biotic soils. *Precambrian Res.* **2020**, *350*, 105948. https://doi.org/10.1016/j.precamres.2020.105948.
62. Wiewióra, A.; Giresse, P.; Petit, S.; Wilamowski, A. A deep-water glauconitization process on the Ivory Coast—Ghana Marginal Ridge (ODP Site 959): Determination of Fe^{3+}-rich montmorillonite in green grains. *Clays Clay Miner.* **2001**, *49*, 540–558.
63. Baldermann, A.; Grathoff, G.H.; Nickel, C. Micromilieu-controlled glauconitization in fecal pellets at Oker (Central Germany). *Clay Miner.* **2012**, *47*, 513–538. https://doi.org/10.1180/claymin.2012.047.4.09.
64. Bansal, U.; Banerjee, S.; Pande, K.; Ruidas, D.K. Unusual seawater composition of the Late Cretaceous Tethys imprinted in glauconite of Narmada basin, central India. *Geol. Mag.* **2019**, *157*, 233–247. https://doi.org/10.1017/s0016756819000621.
65. Odin, G.; Fullagar, P. Chapter C4 Geological Significance of the Glaucony Facies. In *Developments in Sedimentology*; Odln, G.S., Eds.; Elsevier: Amsterdam, The Netherlands, 1988; Volume 45, pp. 295–332. https://doi.org/10.1016/s0070-4571(08)70069-4.
66. Moore, D.M.; Reynolds, R.C. *X-ray Diffraction and the Identification and Analysis of Clay Minerals (No. 549 MOO)*; Oxford University Press: Oxford, UK, 1997.
67. Boulesteix, T.; Solé, J.; Pi, T.; Cathelineau, M. Reappraisal of the GL-O Reference Material for K-Ar Dating: New Insight from Microanalysis, Single-Grain and Milligram Ar Measurements. *Geostand. Geoanal. Res.* **2020**, *44*, 287–306.
68. Pestitschek, B.; Gier, S.; Essa, M.; Kurzweil, H. Effects of Weathering on Glauconite: Evidence from the Abu Tartur Plateau, Egypt. *Clays Clay Miner.* **2012**, *60*, 76–88. https://doi.org/10.1346/ccmn.2012.0600107.
69. Guimaraes, E.M.; Velde, B.; Hillier, S.; Nicot, E. Diagenetic/anchimetamorphic changes on the Proterozoic glauconite and glaucony from the Paranoa group, mid-western Brazil. *Rev. Bras. Geocienc.* **2017**, *30*, 363–366.
70. Baldermann, A.; Warr, L.N.; Grathoff, G.H.; Dietzel, M. The Rate and Mechanism of Deep-Sea Glauconite Formation at the Ivory Coast—Ghana Marginal Ridge. *Clays Clay Miner.* **2013**, *61*, 258–276. https://doi.org/10.1346/ccmn.2013.0610307.
71. Ernst, G.; Schmid, F.; Seibertz, E. Event-Stratigraphie im Cenoman und Turon von NW-Deutschland. *Zitteliana* **1983**, *10*, 531–554.
72. Tiessen, E. Die subhercyne Tourtia und ihre Brachiopoden-und Molluskenfauna. *Z. Dt. Geol. Ges.* **1895**, *47*, 423–533.
73. Gale, A.S.; Mutterlose, J.; Batenburg, S.; Gradstein, F.M.; Agterberg, F.P.; Ogg, J.G.; Petrizzo, M.R. The Cretaceous Period. In *Geologic Time Scale 2020*; Gradstein, F.M., Ogg, J.G., Schmitz, M.D., Ogg, G.M., Eds.; Elsevier: Amsterdam, The Netherlands, 2020; Volume 2; pp. 1023–1086.
74. Hower, J. Some factors concerning the nature and origin of glauconite. *Am. Mineral.* **1961**, *46*, 313–334.
75. Baldermann, A.; Warr, L.N.; Letofsky-Papst, I.; Mavromatis, V. Substantial iron sequestration during green-clay authigenesis in modern deep-sea sediments. *Nat. Geosci.* **2015**, *8*, 885–889. https://doi.org/10.1038/ngeo2542.
76. Abbott, A.N.; Löhr, S.; Trethewy, M. Are Clay Minerals the Primary Control on the Oceanic Rare Earth Element Budget? *Front. Mar. Sci.* **2019**, *6*, 504. https://doi.org/10.3389/fmars.2019.00504.
77. Jeandel, C.; Oelkers, E.H. The influence of terrigenous particulate material dissolution on ocean chemistry and global element cycles. *Chem. Geol.* **2015**, *395*, 50–66. https://doi.org/10.1016/j.chemgeo.2014.12.001.
78. Webb, P. *Introduction to Oceanography*; Roger Williams University: Bristol, RI, USA, 2021.
79. Hedges, J.I.; Keil, R.G. Sedimentary organic matter preservation: An assessment and speculative synthesis. *Mar. Chem.* **1995**, *49*, 81–115. https://doi.org/10.1016/0304-4203(95)00008-f.
80. Jeandel, C. Overview of the mechanisms that could explain the 'Boundary Exchange' at the land-ocean contact. *Philos. Trans. A Math. Phys. Eng. Sci.* **2016**, *374*, 20150287.
81. Kelly, J.C.; Webb, J.A.; Maas, R. Isotopic constraints on the genesis and age of autochthonous glaucony in the Oligo-Miocene Torquay Group, south-eastern Australia. *Sedimentology* **2001**, *48*, 325–338.
82. Dickin, A.P. *Radiogenic Isotope Geology*, 3rd ed.; Cambridge University Press: Cambridge, UK, 2018; pp. 40–66.
83. Smalley, P.; Forsberg, A.; Råheim, A. RbSr dating of fluid migration in hydrocarbon source rocks. *Chem. Geol.* **1987**, *65*, 223–233.
84. Charpentier, D.; Buatier, M.; Jacquot, E.; Gaudin, A.; Wheat, C. Conditions and mechanism for the formation of iron-rich Montmorillonite in deep sea sediments (Costa Rica margin): Coupling high resolution mineralogical characterization and geochemical modeling. *Geochim. Cosmochim. Acta* **2011**, *75*, 1397–1410. https://doi.org/10.1016/j.gca.2010.11.026.
85. O'Brien, C.L.; Robinson, S.A.; Pancost, R.D.; Damsté, J.S.S.; Schouten, S.; Lunt, D.J.; Alsenz, H.; Bornemann, A.; Bottini, C.; Brassell, S.C.; et al. Cretaceous sea-surface temperature evolution: Constraints from TEX86 and planktonic foraminiferal oxygen isotopes. *Earth-Sci. Rev.* **2017**, *172*, 224–247. https://doi.org/10.1016/j.earscirev.2017.07.012.
86. Beckmann, B.; Flögel, S.; Hofmann, P.; Schulz, M.; Wagner, T. Orbital forcing of Cretaceous river discharge in tropical Africa and ocean response. *Nature* **2005**, *437*, 241–244. https://doi.org/10.1038/nature03976.